Hindawi
Journal of Nanomaterials
Volume 2018, Article ID 6939621, 15 pages
https://doi.org/10.1155/2018/6939621

Research Article

Piezoelectric and Dielectric Characterization of MWCNT-Based Nanocomposite Flexible Films

S. Banerjee, W. Du, U. Sundar, and K. A. Cook-Chennault

Department of Mechanical and Aerospace Engineering, Rutgers University, Piscataway, NJ 08854-8053, USA

Correspondence should be addressed to K. A. Cook-Chennault; cookchen@soe.rutgers.edu

Received 7 April 2018; Accepted 12 July 2018; Published 30 September 2018

Academic Editor: Avinash Baji

Copyright © 2018 S. Banerjee et al. This is an open access article distributed under the Creative Commons Attribution License, which permits unrestricted use, distribution, and reproduction in any medium, provided the original work is properly cited.

PZT-epoxy-multiwalled carbon nanotube (MWCNT) flexible thick film actuators were fabricated using a sol-gel and spin coat and deposition process. Films were characterized in terms of their piezoelectric and dielectric properties as a function of MWCNT volume fraction and polarization process. Correlations between surface treatment of the MWCNTs and composite performance were made. The surface morphology and filler distribution were observed with the aid of SEM and TEM images. The volume fraction of PZT was held constant at 30%, and the volume fraction of MWCNTs varied from 1% to 10%. Two forms of dielectric polarization were compared. Corona discharge polarization induced enhanced piezoelectric and dielectric properties by a factor of 10 in comparison to the parallel-plate contact method (piezoelectric strain coefficient and dielectric constant were 0.59 pC/N and 61.81, respectively, for the parallel-plate contact method and 9.22 pC/N and 103.59 for the corona polarization method, respectively). The percolation threshold range was observed to occur at a MWCNT volume fraction range between 5% and 6%.

1. Introduction

Piezoelectric materials are used as sensors, actuators, and transducers for many applications such as quality assurance [1, 2], process control [3–5], industrial and automotive systems [6–9], medical diagnostics [10, 11], aviation and structural health monitoring [12–15], biologically engineered scaffolds [16], and embedded passive devices in consumer electronics [17–19]. However, the brittle nature of homogenous ceramic piezoelectric materials limits their operational strains ($\sim 8 \times 10^{-6}$ to 6×10^{-4}) [20–22], cycle life when subjected to high strain/deformation conditions [23], and ability to be formed into synclastic and complex forms. These challenges often restrict the use of these materials in advanced applications that require sensors that are electromechanically tuned to host structures, while maintaining high sensitivity and reliability over wide frequency ranges.

Composites comprised of piezoelectric ceramic fillers embedded within a matrix material have been proposed for many applications such as hybrid energy systems [24, 25], battery separator materials [26], energy harvesting, energy conversion storage [6, 24, 25, 27], and capacitors [35, 36]. Two-phase polymer matrix-based composites such as PZT-epoxy [37], comprised of piezoelectric particles embedded within a continuous polymer matrix, have attracted much attention due to their flexibility, ease of processing, and use in embedded passive devices. Integration of embedded passive components into printed circuit boards generally results in enhanced electrical performance of the device, improved reliability, reduction of device size, faster switching speed, and lower production costs [28]. Piezoelectric polymer composites are promising materials because of their excellent tailored properties [6, 25]. These materials have many advantages including high electromechanical coupling factors [38–40], low acoustic impedance [41, 42], mechanical flexibility [43, 44], a wide broad bandwidth [45, 46], and low mechanical quality factor [25, 47]. The mechanical, electrical, and acoustic properties of these materials can also be tailored according to the nature of application as a function of composition of the composite material [48–51].

On the other hand, two-phase piezoelectric-epoxy composites suffer from poor electrical, dielectric, and piezoelectric properties due to the insulating nature and low dielectric constant of the epoxy matrix, which decreases

Table 1: Unique mechanical and electrical properties of carbon nanotubes as compared to other electrically conductive materials [30, 61–71].

Material	Density (g/cm^3)	Young's modulus (TPa)	Yield strength (GPa)	Electrical resistivity (10×10^{-8} Ohm·m)	Electrical conductivity (10×10^6 S/m)
Single-walled carbon nanotube (bundles)	1.3–2	0.9–1.1 (variation due to tube diameter)	3–25 (variation due to tube diameter)	1.0–10.0	1–10
Multiwalled carbon nanotubes (bundles)	1.3–2	0.8–1.5 (variation due to the number of tubes)	20–60 (variation due to the number of tubes)	1.0–10.0	1–10
Silver	10.4	0.083	0.054	1.6	63
Copper	8.9	0.125	0.069	1.7	59.6
Stainless Steel	7.8	0.2	4.1	73.0–78.0	2.0–8.5
Carbon fiber	1.7–2	0.2–0.6	1.7–5	80.0–163.0	1.45
Gold	19.4	0.076–0.081	0.10–0.22	2.3	44.2
Aluminum	2.7	0.069	0.007–0.011	2.7	36.9

Table 2: Variation of percolation threshold with the variation in aspect ratio of the electrically conductive inclusion (CNTs).

Electrically conductive filler (aspect ratio (AR))	Composite (fabrication method)	Percolation (volume fraction %)
MWCNT (AR = 400) [72]	MWCNT-PVDF (sol-gel and hot molding)	1.0%
MWCNT (AR~100) [72]	MWCNT-PMMMA (compression molding)	2.4%
SWCNT (AR~100) [34]	SWCNT-PMMA (compression molding)	3.4%
SWCNT (AR~1000) [73]	SWCNT-PZT-PMMA (solution casting)	0.8%
CNT (AR~100) [74]	CNT-Alumina (colloidal processing)	2.2%
MWCNT (AR~100) [75]	MWCNT-Epoxy (sol-gel sintering)	2–2.75%
Double-walled CNTs (AR > 1000) [76]	CNT-Epoxy (vacuum sintering)	0.25%
MWCNT (AR > 100) [60]	MWCNT-Epoxy (sol-gel sintering)	2.5%
CNT (AR~200–1000) [77]	CNT-Epoxy (sol-gel sintering)	0.5–1.5%
MWCNT (AR~1000) [78]	MWCNT-Epoxy (sol-gel sintering)	0.8%
MWCNT (AR~500–2000) [79]	Carbonized MWCNT/resorcinol-formaldehyde xerogels (sol-gel polymerization)	1.6–3.18%
MWCNT (AR~62) [80]	MWCNT/thermoplastic elastomer (melt blending)	9.0%
MWCNT (AR~116) [80]	MWCNT/thermoplastic elastomer (melt blending)	10%
MWCNT (AR~437) [80]	MWCNT/thermoplastic elastomer (melt blending)	3.5%

the polarization of the piezoelectric phase [52, 53]. The nonuniform distribution of the ferroelectric phase in the polymer matrix can also cause clustering and agglomerations [6, 54], which can contribute to the insulative nature of the composite.

The electrical properties of the matrix may be enhanced with the incorporation of electrically conductive inclusions [28, 55] such as carbon nanotubes (CNTs) [32, 56]. The mechanical and electrical properties of typical filler materials are presented in and compared to the properties of carbon nanotubes in Table 1. Many researchers have reported that the conductivity of the matrix component of the composite is enhanced by inclusion of electrically conductive fillers [57, 58]. However, less is known about interrelationship between the composite processing technique and the morphology and properties of the electrically conductive particles, which dictate the effective piezoelectric and dielectric properties of the composite material [6, 32]. Furthermore, the inclusion of electrically conductive fillers leads to additional concerns such as the percolation of the conductive filler [40, 59, 60], which is dictated by the distribution of the filler within the matrix and the aspect ratio of the filler as indicated by the variability in percolation values indicated in Table 2.

In this work, the mechanisms that influence the piezoelectric and dielectric properties of three-phase composites (PZT, epoxy, and MWCNTs) are investigated as a function of the volume fraction of MWNTs with the aim at understanding the influence of polarization technique and percolation range on the aforementioned properties. The films were characterized in terms of their dielectric spectra, piezoelectric strain coefficients, dielectric loss (tan δ), and impedance spectra. And the distribution of the fillers in the matrix, interfacial phase interactions, and preprocessing of MWCNTs and PZT were also studied with the aid of a scanning electron microscopy (SEM) and transmission electron microscopy (TEM) images to ascertain the degree of separation of particles, particle morphology, composite porosity, and agglomeration.

Table 3: Overview of the piezoelectric, dielectric, and physical properties of PZT and epoxy.

Material	Dielectric constant (ε)	Piezoelectric strain d_{33}/d_{31} (pC/N)	Dielectric loss (tan δ)	Young's modulus (10^{10} N/m^2)	Density (kg/m^3)
PZT (APC International, 855, Navy VI)	3300 (at 1 kHz)—from the manufacturer (606.70—measurement in the lab at the same frequency)	400/175	≤2.50	6.4	7500
Epoxy (Electron Microscopy Sciences, DGEBA, EMS 1232)	8.239 (at 1 kHz)—from the manufacturer (12.23 from measurement in the lab at the same frequency)	NA/NA	<1	0.15–0.20	1160 (in wet state)

2. Methodology

2.1. Material Properties. Three-phase piezoelectric (0-3-0) composites that comprised multiwalled carbon nanotubes (MWCNTs), lead zirconate titanate ($Pb(Zr_xTi_{(1-x)})O_3$; 855, Navy VI) (purchased from APC International), and a two-part epoxy—DGEBA, Epofix™ cold-setting embedding resin (purchased from Electron Microscopy Sciences), were fabricated via a modified sol-gel and spin coat and deposition process onto stainless-steel bottom electrodes. The cold-setting resin was a two-part epoxy that consisted of a bisphenol-A-diglycidylether-based resin and a triethylenetetramine-based hardener. The average aspect ratio of the MWCNTs was determined from TEM images to be ~461. The piezoelectric, dielectric, and physical properties of the PZT and epoxy are presented in Table 3.

2.2. Composite Film Preparation. An overview of the thick film fabrication process is provided in Figure 1. It is well known that the distribution of dielectric fillers and conductive fillers within an insulative matrix influences the macroscopic dielectric and piezoelectric characteristics of the thick composite films [32, 35, 37, 31]. Hence, the PZT and MWNT fillers were preprocessed. The PZT filler was preprocessed using the method described in [30] and then mixed with the bisphenol-A-diglycidyl ether part of the two-part epoxy and sonicated for four hours. A study was performed to ascertain the appropriate sonication time for the surface treatment of the MWCNTs in ethanol (200 proof, Sigma-Aldrich) in the ultrasonicator (procedure described in Section 2.3).

After the MWCNTs were surface treated, they were mixed with the mixture of PZT and epoxy, thus forming the sol (nonmacroscopic particles in solution) and a gel (bushy structures as clusters and agglomeration pockets of PZT-epoxy and MWCNTs). The organic residues that were left behind by the gradual evaporation of the ethanol bound the different phases in the mixture during the desiccation step that occurred for four hours. The binder component of the epoxy was then added to the mixture, and the solution then sonicated for an additional half hour. The sol-gel formed was spin coated onto a stainless-steel substrate using the Laurell WS-650-23NPP spin coater. The stainless-steel substrate was 1.5 cm × 2.5 cm and 20 μm thick. The spin coat process included incremental increases by 100 rpm, until a final speed of 1000 rpm was achieved. The substrate is coated

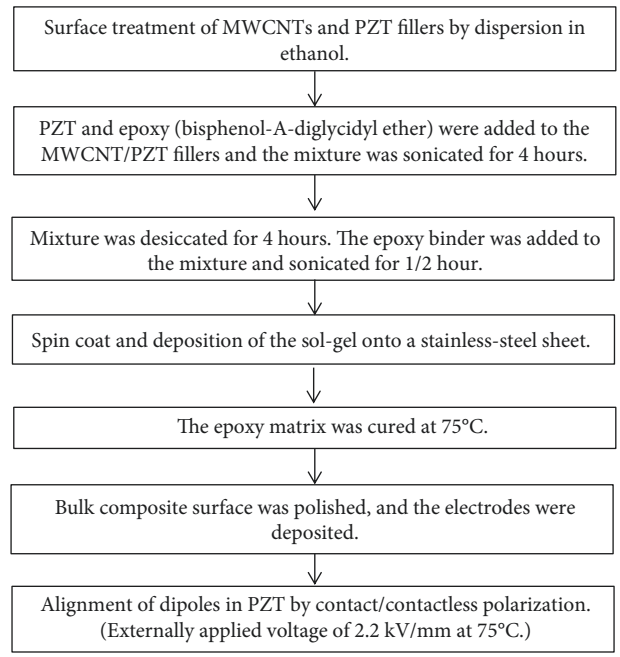

Figure 1: Overview of the thick film fabrication process.

with a three-phase PZT-Epoxy-MWNCT composite material of thickness ~150 μm. The film was then allowed to cure on a hot plate at 75°C (glass transition temperature of the epoxy) for eight hours and then subsequently polarized via a parallel-plate contact or a corona discharge method. The volume fraction of PZT was held constant at 30%, while the volume fraction of MWCNTs varied from 1.0% to 10% to optimize and to identify the percolation threshold. The piezoelectric strain coefficients, d_{33} and d_{31}, dielectric and impedance spectra, and conductivity were determined as a function of polarization process, i.e., contact parallel plate or corona plasma and volume fraction of MWCNTs.

The parallel-plate contact polarization method was achieved by placing the film in between the top and the ground base plates in a dielectric medium (silicone oil) as shown in Figure 2 and applying an external electric field of 2.2 kV/mm. The composite is heated to the glass transition temperature of the matrix phase, and an electric field is applied at the electrodes. The corona discharge polarization method is shown in Figure 3. This process involves the application of an electric field via a needle that is held at a certain

distance away from the composite material. A voltage is applied to the needle and the base (ground) plate, which is heated to its glass transition temperature of the epoxy. When the needle reaches the ionizing potential of the surrounding air, ionic species are generated and attracted towards the ground base plate. When a sufficient surface charge density is reached, the ions flow towards the base plate through the thickness of the composite material leading to the polarization of the dielectric film.

2.3. Surface Treatment of MWCNTs. A study to examine the amount of time required to separate the agglomerated MWCNTs, which arrive clumped together and attached to a cathode, was performed. The MWCNTs received from the manufacturer are cathode deposited and in the form of pellets. SEM and TEM micrographs of the MWCNTs were used to determine the optimal time for minimal agglomeration of MWCNTs and maximum dispersion of MWCNTs within the epoxy matrix. Thus, the MWCNTs were dispersed in ethanol and sonicated for specified amounts of time, (30 minutes, 2, 3, and 4 hours) and then deposited on the SEM studs and TEM grids. After the ethanol evaporated, images of the MWCNTs were taken. In addition, samples that were made using MWCNTs sonicated at the different times were fabricated and analyzed with the aid of SEM and TEM images. The SEM micrographs can be used to visualize the dispersion of the MWCNT clusters. The appropriate sonication time was determined by examining the average particle size and separation of particles with the aid of the SEM images. The high-resolution TEM images give insight into the size, shape, and morphological structure of the MWCNTs after exposure to ethanol and sonication for specified amounts of time.

2.4. Sample Characterization. A piezometer was used to measure the dielectric constant, dielectric loss tangent, and the piezoelectric strain coefficients (d_{33} and d_{31}) at a frequency of 110 Hz. Impedance spectroscopy and dielectric spectroscopy of the bulk and thick film composites are performed by using the HP4194A Impedance Analyzer at varying frequencies from 100 Hz to 20 MHz. The fractured surface morphology and electron dispersion spectroscopy (EDS) of the samples are studied with the help of the scanning electron microscope (FESEM ZEISS 982) and the field emission transmission electron microscope (TEM JEOL 2010F).

3. Results and Discussion

3.1. SEM and TEM Characterization of MWCNTs and Composite Films. The appropriate sonication time for the surface treatment of the MWCNTs in ethanol was determined by examining the average particle size and separation of particles using SEM micrograph images and TEM images. MWCNTs that were produced by arc discharge cathode deposition were ultrasonicated in 40 ml of ethanol for time intervals equal to 30 minutes, 2 hours, 3 hours, 4 hours, and 8 hours. The surface-treated MWCNTs were then incorporated into 0-3-0 composite films having 3%, 6%, and 9% volume fraction of MWCNTs.

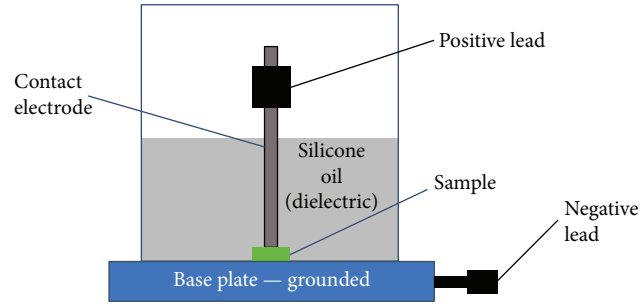

Figure 2: Parallel-plate contact polarization process where the film is submerged in a dielectric silicon oil and an external electric field is applied.

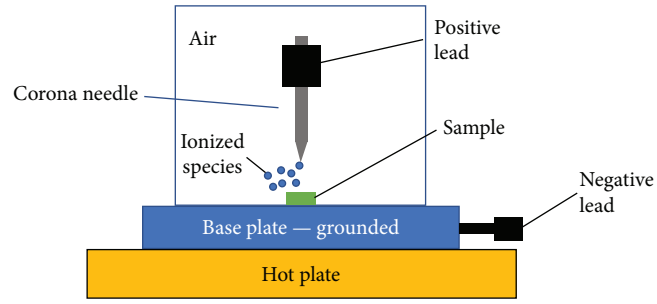

Figure 3: The corona discharge poling method is shown where the needle ionizes the volume of air surrounding it. The ions on the top surface of the composite material are attracted towards the ground base plate.

MWCNTs that were treated for 30 minutes in ethanol and the associated piezoelectric composite films are shown in Figure 4. In Figure 4(a), MWCNTs that were surface treated for 30 minutes in ethanol are shown at a magnification of 2.41 K. It is evident that the degree of vibration energy was not sufficient enough to deagglomerate the MWCNT clusters that are held together by van der Waals forces. Hence, as expected, the MWCNTs remained agglomerated (>20 μm in scale) throughout the fabrication process described in Figure 1, where films comprised of 3%, 6%, and 9% which are shown in Figures 4(a)–4(c)), respectively. The average agglomeration size for each volume fraction was determined with the aid of ImageJ software for 3%, 6%, and 9% volume fraction of MWCNTs, respectively, as indicated in Table 4. SEM images of ethanol surface treatment for 2 hours, 3 hours, 4 hours, and 8 hours are shown in Figures 5–8. The degree of MWCNT agglomeration decreases as a function of ultrasonication time in ethanol from 30 minutes to 4 hours as indicated by the SEM images and particle average size range provided in Table 4. The degree of MWCNT separation reaches a plateau beyond 4 hours as shown in Table 4 and through the observation of composite films in Figures 4–8.

An image analysis of MWCNT clusters in Figure 4 indicates that the average size of the clusters are 50, 60, and 65 μm, for volume fractions of 3%, 6%, and 9%, respectively. In Figure 5, the dispersion of the MWCNT pellets after ultrasonication in ethanol for 2 hours is depicted, where the

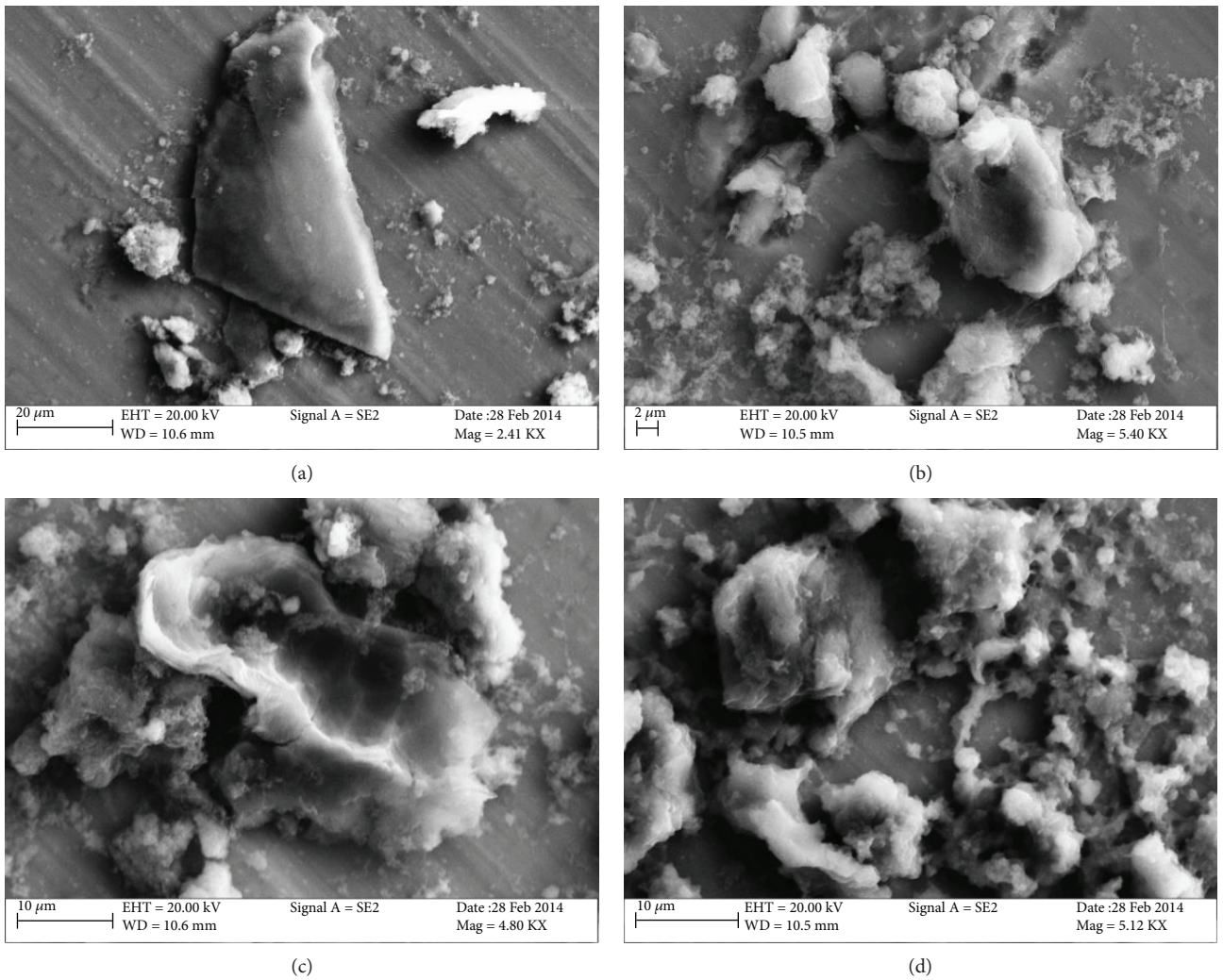

Figure 4: SEM micrograph images of (a) agglomerated MWCNTs after ultrasonication with 40 ml of ethanol for 30 minutes. Piezoelectric composite films with MWCNT content equal to (b) 36.4 mg (3% in volume of the final PZT-Epoxy-MWCNT mixture), (c) MWCNT = 72.9 mg (6% in volume of the composite PZT-Epoxy-MWCNT mixture), and (d) MWCNT = 109.35 (9% in volume of the final composite mixture).

average cluster size is ~15 μm, ~16.7 μm, and 17.5 μm for volume fractions of 3%, 6%, and 9% of MWCNTs, respectively. As expected, the average particle cluster size decreases as the sonication time increases from 30 minutes to 2 hours. Similarly, the size of the MWCNT cluster size continues to decrease with sonication time as it is increased from 2 hours to 3 and then 4 hours.

Figure 6 depicts the dispersion of the MWCNTs within the composite film, where the MWCNTs were treated with ethanol for 3 hours. The average MWCNT cluster sizes were 1.25 μm, 1.36 μm, and 1.44 μm, for MWCNT volume fractions of 3%, 6%, and 9%, respectively, as indicated by the ImageJ software. The images also indicate that for higher volume fractions of MWCNTs, more aggregated clusters of nanotubes are present. Extension of the ultrasonication time from 3 hours to 4 hours leads to reduced agglomerations of the MWCNTs as shown in Figure 7. The dispersion of MWCNT bundles that have been ultrasonicated in ethanol for 4 hours is shown in SEM micrographs in Figure 7.

Image analysis indicates that the sizes of the particle bundles in Figure 7 are 326 nm, 340 nm, and 345 nm for MWCNT volume fractions of 3%, 6%, and 9%, respectively. An analysis of the SEM micrographs in Figure 8 at a sonication time of 8 hours shows that the average size of the MWCNT bundles is similar to the values in Figure 7, where, for a sonication time of 8 hours, the nanocluster sizes are 338 nm, 347 nm, and 347 nm for MWCNT volume fractions of 3%, 6%, and 9%, respectively. The similarity of values between ultrasonication times of 4 and 8 hours confirms that the ultrasonic time for the ethanol treatment of the MWCNTs is 4 hours. Hence, a sonication time of 4 hours was used for the surface treatment of MWCNTs.

The transmission electron microscope (TEM) images are also provided to observe the size and aggregated masses of MWCNTs. TEM images of MWCNTs that have been subjected to a 4-hour ethanol ultrasonic bath are shown in Figure 9. The diffraction patterns in this figure show the presence of multiple rings, namely, 4 rings, which can be

Table 4: Overview of the size range of surface modified MWCNT clusters as a function of treatment time and volume fraction in the piezoelectric thick film.

Ultrasonication time	Volume fraction of MWCNTs	Associated SEM figure	Size range of MWCNT cluster
30 minutes	0.03	Figure 4(a)	50 μm
	0.06	Figure 4(b)	60 μm
	0.09	Figure 4(c)	65 μm
2 hours	0.03	Figure 5(a)	15 μm
	0.06	Figure 5(b)	16.7 μm
	0.09	Figure 5(c)	17.5 μm
3 hours	0.03	Figure 6(a)	1.25 μm
	0.06	Figure 6(b)	1.36 μm
	0.09	Figure 6(c)	1.44 μm
4 hours	0.03	Figure 7(a)	326 nm
	0.06	Figure 7(b)	340 nm
	0.09	Figure 7(c)	345 nm
8 hours	0.03	Figure 8(a)	331 nm
	0.06	Figure 8(b)	338 nm
	0.09	Figure 8(c)	347 nm

attributed to the different 2D graphite sheets rolled up in the form MWCNTs. The structure of the MWCNTs with the rings in the diffraction pattern and their morphology in the TEM micrographs are consistent with those found in the literature [81, 82]. TEM images of the composite that is comprised of a MWCNT volume fraction of 0.06 (6%) are depicted in Figure 10. In Figure 10(a), a diffraction pattern of the MWCNTs is shown, where the rings and spots are similar to those observed in Figure 9. In Figure 10(b), a TEM micrograph of the composite thick film is depicted, which shows three MWCNTs embedded in the epoxy matrix alongside polycrystalline PZT inclusions. The MWCNT inclusions shown in Figure 10(b) appear to be twisted and curled due the stresses developed during the sol-gel mixing and the spin coating processes.

Three-phase thick films with MWCNT volume fractions equal to 4% and 6% are shown in Figure 11. Figures 11(a) and 11(b) depict SEM micrographs of the fractured surfaces of the composite thick films, which indicate adhesion of the film onto the stainless steel and fairly smooth surfaces. In Figures 11(c) and 11(d), SEM micrographs of the piezoelectric composite are shown, where the PZT circular-shaped clusters and smaller bundles of MWCNTs are seen to be distributed in the epoxy matrix.

3.2. Piezoelectric, Electrical, and Dielectric Characterization. The piezoelectric and dielectric characteristics of the three-phase PZT-Epoxy-MWCNT thick film composites were examined with the aid of a piezometer and a HP4194A impedance analyzer. Films were polarized via the parallel-plate contact or the corona plasma discharge method. The thick films were correlated to the physical properties described in Section 3.1.

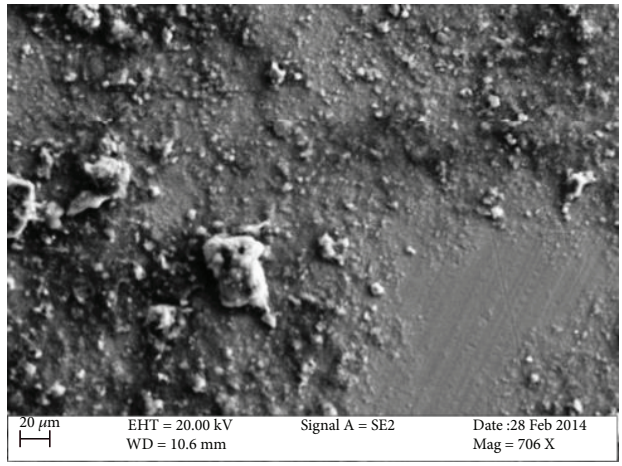

(a)

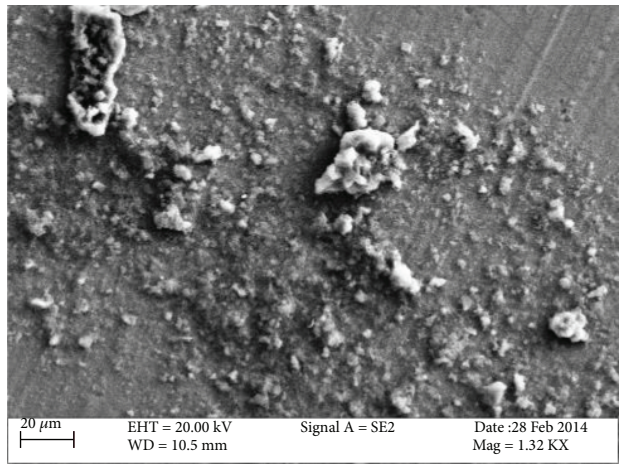

(b)

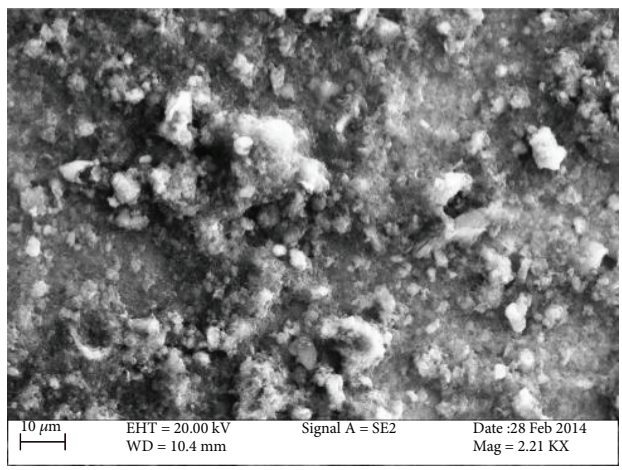

(c)

Figure 5: SEM micrograph images of the dispersion of MWCNTs that have been ultrasonicated in ethanol for 2 hours at (a) MWCNT = 36.4 mg (MWCNT 1), (b) MWCNT = 72.9 mg (MWCNT 2), and (c) MWCNT = 109.35 (MWCNT 3) show smaller agglomerations of MWCNT clusters than the MWCNT clusters treated for 30 minutes.

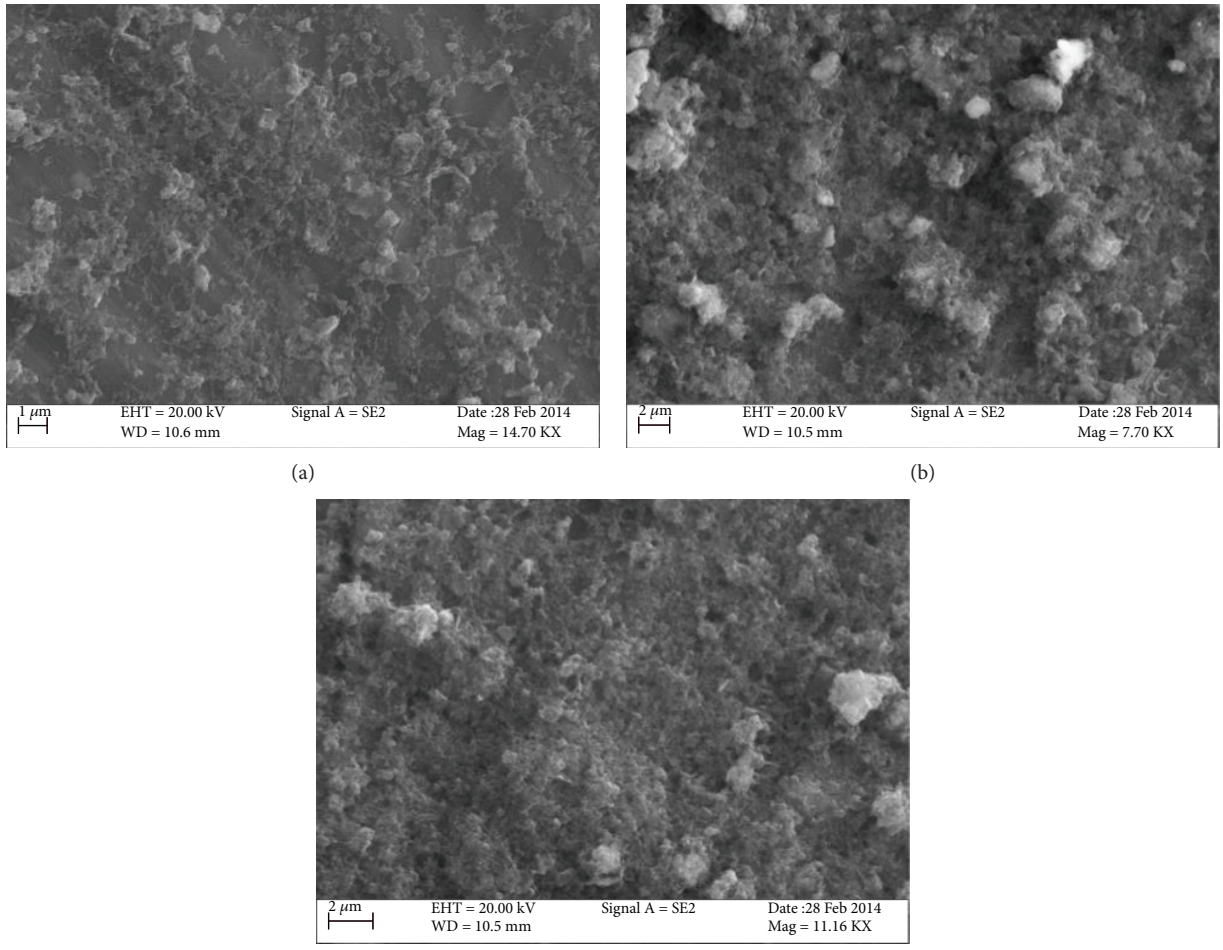

Figure 6: SEM micrograph images of the dispersion of MWCNTs that have been ultrasonicated in ethanol for 3 hours at (a) MWCNT = 36.4 mg (MWCNT 1), (b) MWCNT = 72.9 mg (MWCNT 2), and (c) MWCNT = 109.35 (MWCNT 3) show clouds of MWCNT clustered together.

The capacitance and effective dielectric constant films (volume fraction of PZT = 30%) that were polarized using the contact method are plotted as a function of MWCNT volume fraction in Figures 12 and 13. From these figures, it can be seen that the capacitance and the dielectric constant of the thick films increase with the increase in the volume fraction of the MWCNT inclusions. For example, the capacitance and dielectric constant are ~3 pF and ~39 and ~5 pF and ~61 for MWCNT volume fractions of 1% and 5%, respectively. The dielectric loss (tan (δ)) of the composite is plotted as a function of MWCNT volume fraction in Figure 13. The value of tan (δ) increases moderately from 0.025 to 0.035 for an increase in MWCNT volume fraction from 1% to 5%, and substantially from 0.035 to 0.085 at a MWCNT volume fraction of 6%. These increases in the dielectric constant and dielectric loss are attributed to the higher volume fraction of MWCNTs. The higher density of MWCNTs enhances the electron transport due to the formation of conductive pathways within the matrix, which enhances the effect on the polarization process. Similarly, the piezoelectric strain coefficients, d_{33} and d_{31}, increase as a function of the volume fraction of MWCNTs shown in Figure 14. The piezoelectric strain coefficients were measured at a frequency of 110 Hz and force of 0.25 N. The strain coefficient, d_{33}, increases from 0.06 to 0.45 pC/N with an increase in MWCNT volume fraction from 1% to 5%. A similar trend is seen with the transverse piezoelectric strain coefficient, d_{31}, which increases from ~0.24 to ~0.35 pC/N with an increase in MWCNT volume fraction from 1% to 4%. The increase in the piezoelectric strain coefficients (d_{33} and d_{31}) with the increase in the MWCNT volume fraction can be attributed to the increase in polarization of the thick film composite due to the increased conductivity by the MWCNT inclusions as confirmed in Figure 18.

On the other hand, d_{33} and d_{31} drop to ~0.09 pC/N and d_{31} ~0.20 pC/N, respectively, after the volume fraction of MWCNTs increases to 6%. A sharp rise in tan (δ) from ~0.03 to ~0.08 is also observed for a change in MWCNT volume fraction from 1% to 5%. This increase is also coupled with a steep increase in the capacitance and dielectric constant, i.e., from ~5 pF and ~61 to ~6 pF and ~76, respectively. This may happen due to electron tunneling along localized conductive pathways formed by MWCNT agglomerations along the thickness of the composite thick film.

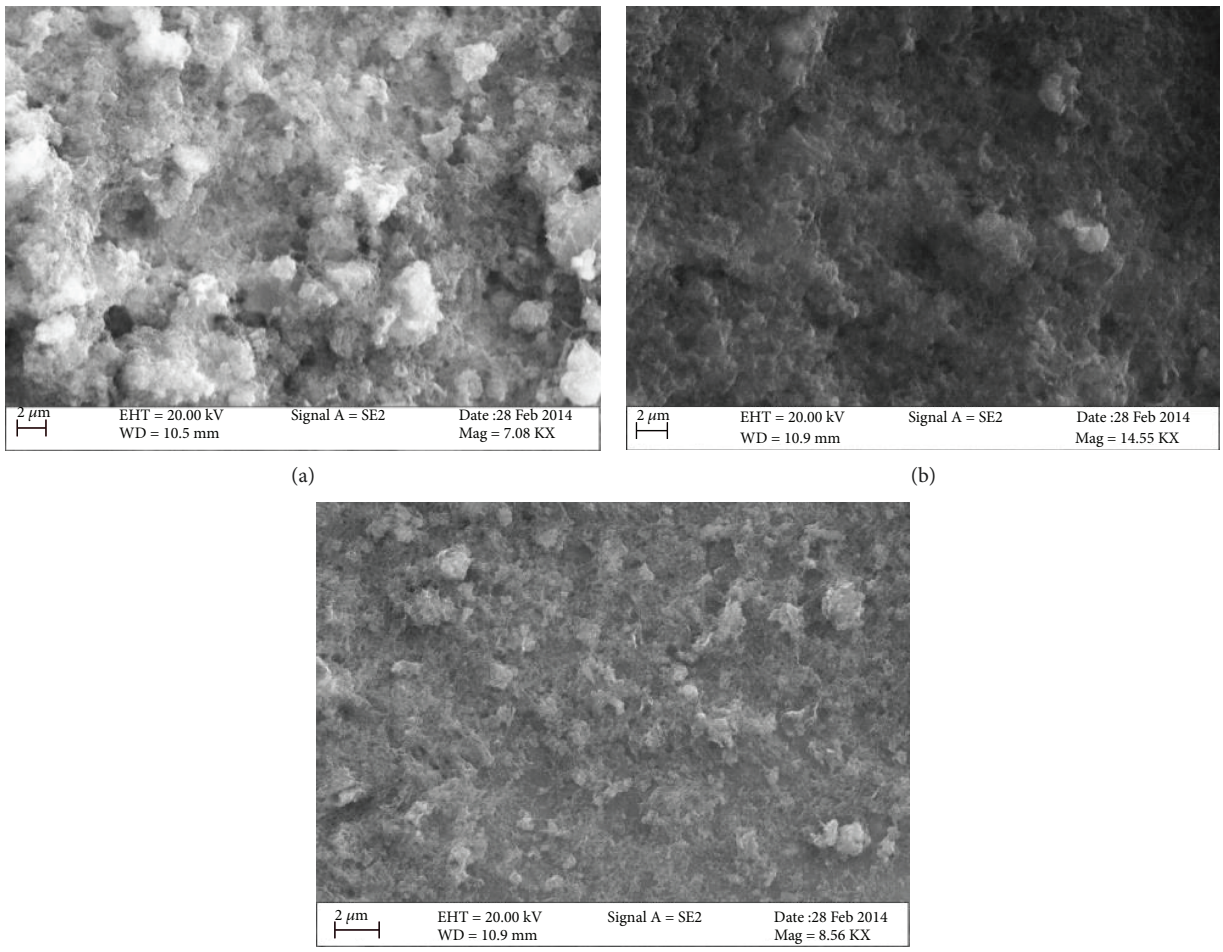

Figure 7: SEM micrograph images of the dispersion of MWCNTs that have been ultrasonicated in ethanol for 4 hours at (a) MWCNT = 36.4 mg (MWCNT 1), (b) MWCNT = 72.9 mg (MWCNT 2), and (c) MWCNT = 109.35 (MWCNT 3) show smaller agglomerations of MWCNT clusters.

This phenomenon is observed in the three-phase composite micron-sized film around a MWCNT volume fraction of around 5-6%. This is also indicated by the sharp increase in the tan (δ) which is caused by a sharp rise in conductivity due to the MWCNT conductive pathways.

Capacitance, ε', and tan (δ) values of the PZT-Epoxy-MWCNT composite with corona discharge poling are plotted as a function of increasing values of MWCNT volume fraction in Figures 15 and 16. This trend is similar to the trend observed for the contact polarized samples. For example, the capacitance and dielectric constants increase from ~6 pF and ~70 to ~9 pF and ~115 for an increase in MWCNT volume fraction from 1% to 5%. For MWCNT volume fractions between 6% and 10%, a nearly linear positive relationship exists. For example, as the MWCNT volume fraction increases from 1% to 10%, the capacitance and dielectric constant increases from ~3 pF and ~50 to ~5 pF and ~68. The tan (δ) values also increase with MWCNT volume fraction. For example, tan (δ) increases from ~0.001 to ~0.004 for a change in MWCNT volume fraction from 1% to 5%, and then from ~0.013 to ~0.023 for MWCNT volume fractions of 6% and 10%, respectively, as shown in Figure 15. d_{33} and d_{31} values of the corona polarized composites are plotted with increasing MWCNTs as shown in Figure 17. For example, the longitudinal and transverse piezoelectric strain coefficients are d_{33}~6 pC/N and d_{31}~3 pC/N to d_{33} ~11 pC/N and d_{31}~9 pC/N for MWCNT volume fractions of 1% and 5%, respectively. Similar to the contact polarized samples, the piezoelectric strain coefficients of the corona polarized samples sharply decrease from a volume fraction of 5% to 6% for the MWCNTs, i.e., d_{33}~8 pC/N and d_{31}~3 pC/N. The same change in MWCNT volume fraction causes sharp increases in the capacitance and dielectric constant values, i.e., C~18 pF and ε'~180, respectively. These changes indicate that the location of the percolation threshold is around this region.

These results indicate that the corona polarization technique is more effective than the contact polarization method for the nanocomposites. This can be seen by the enhanced values of ε and the strain coefficients d_{33} and d_{31} for all volume fractions of MWCNT ranging from 1% to 5% (below the percolation threshold). The increase in the strain coefficients is due to the increase in effectiveness of the polarization process. The dielectric constant, which is measured in

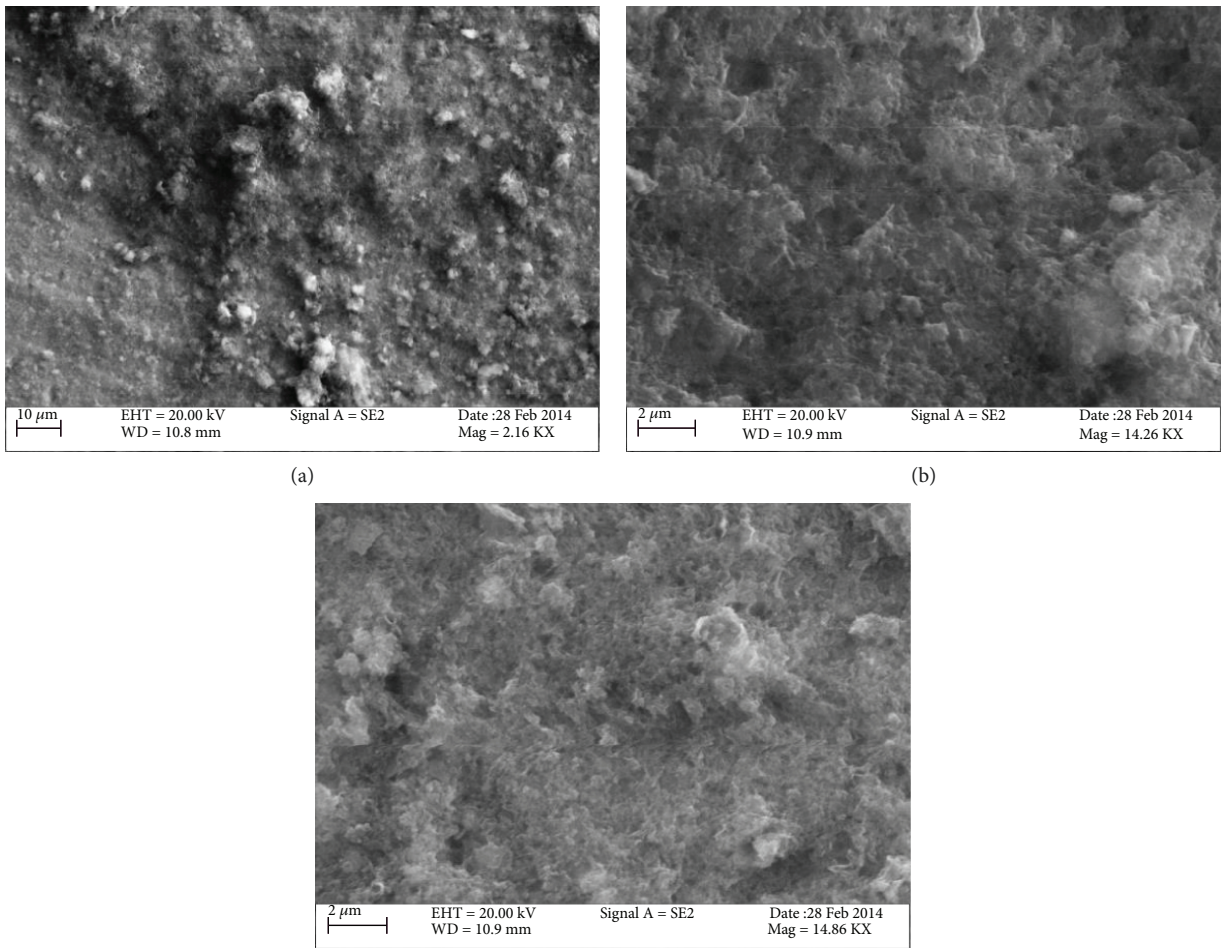

Figure 8: SEM micrograph images of the dispersion of MWCNTs that were ultrasonicated in ethanol for 8 hours at (a) MWCNT = 36.4 mg (MWCNT 1), (b) MWCNT = 72.9 mg (MWCNT 2), and (c) MWCNT = 109.35 (MWCNT 3) show similar MWCNT cluster size as observed for a sonication time of 4 hours.

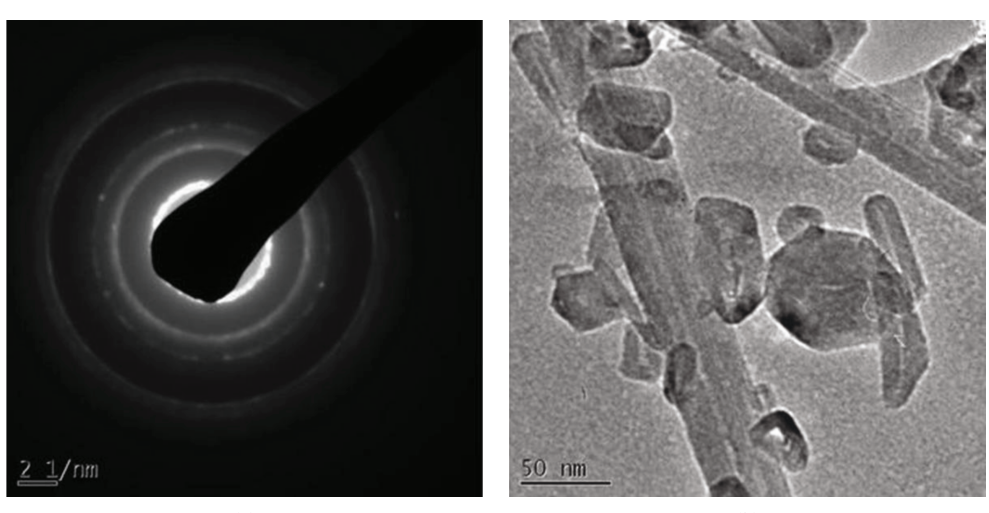

Figure 9: (a, b) Diffraction pattern and TEM images of MWCNTs dispersed in ethanol after a sonication time of 4 hours. The cylindrical ring-like structures of the MWCNTs are present in (a). Even after sonication in ethanol, the TEM images indicate that some forms of agglomeration of MWCNTs still exist.

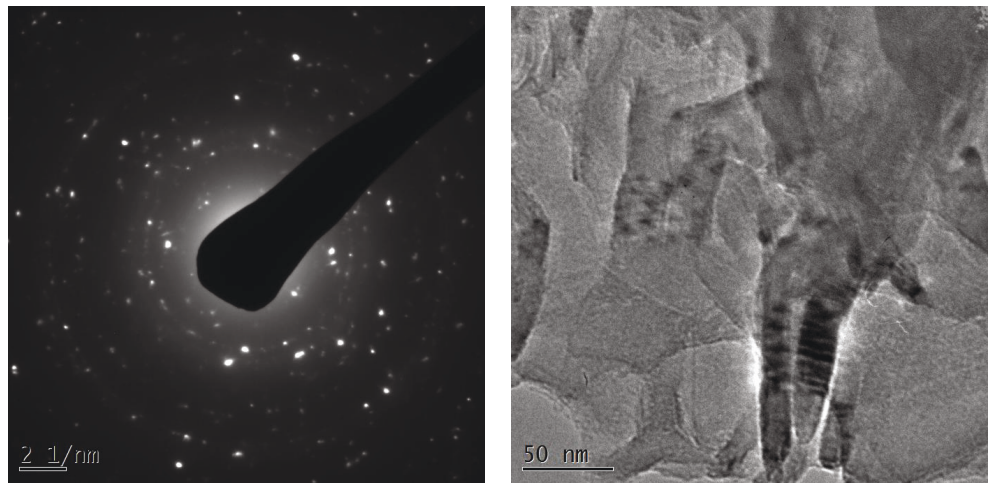

(a) (b)

Figure 10: (a) Diffraction pattern of the PZT-Epoxy-MWCNT thick film composite with a MWCNT volume fraction of 0.06 (6%) showing rings and spots similar to Figure 9 and (b) TEM micrograph of the composite thick film shows three MWCNTs embedded in the epoxy matrix.

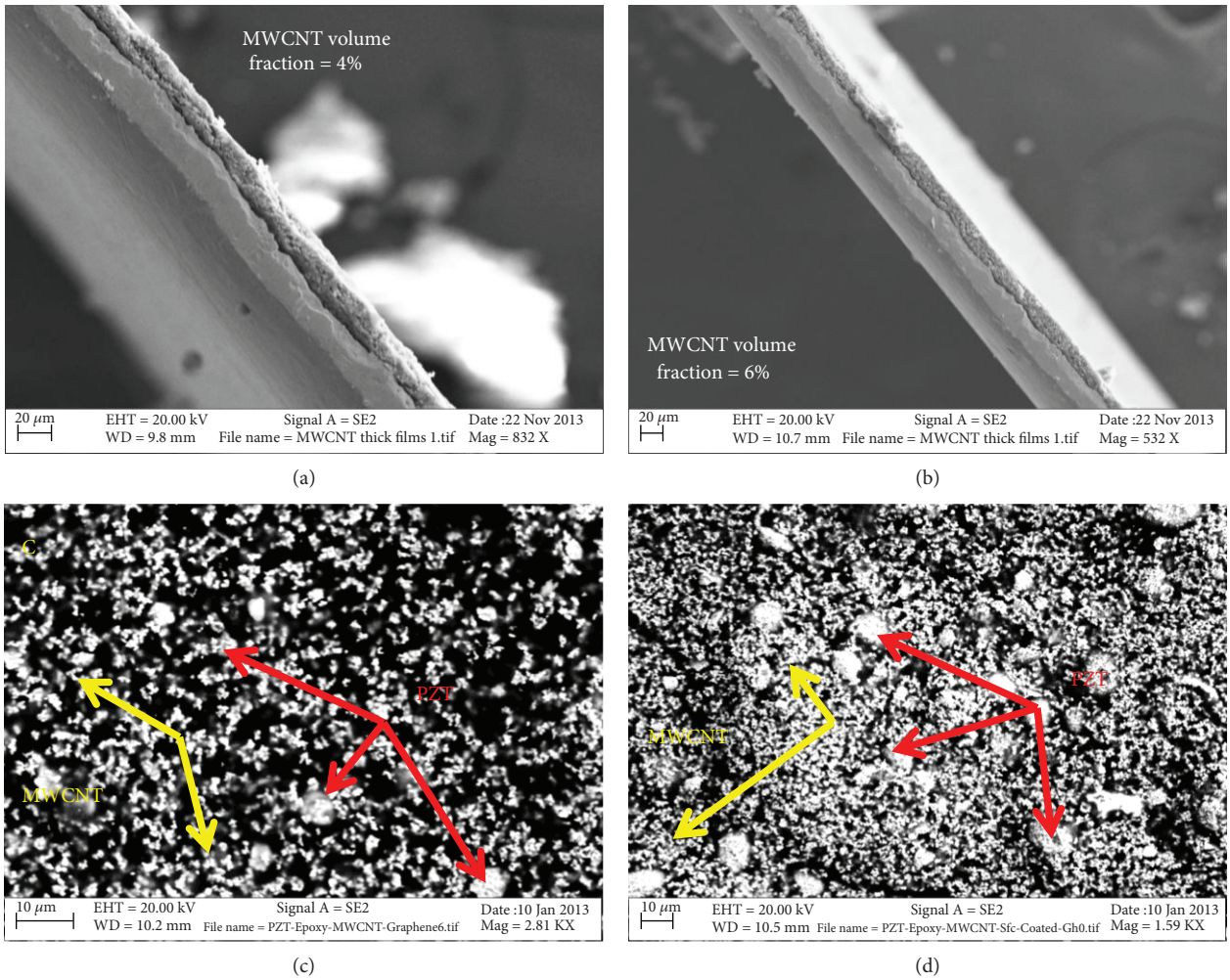

(a) (b)

(c) (d)

Figure 11: Cross-sectional SEM micrograph of a PZT-Epoxy-MWCNT thick film with MWCNT volume fractions of (a) 0.04 (4%) and (b) 0.06 (6%) showing the thick film of thickness ~150 μm spin coated over a flexible stainless substrate of thickness 20 μm. (c, d) The SEM micrographs of the fractured surface of the three-phase composite with MWCNT volume fractions of 0.04 (4%) and 0.06 (6%). They show the distribution of the PZT clusters and MWCNT clusters in the epoxy matrix.

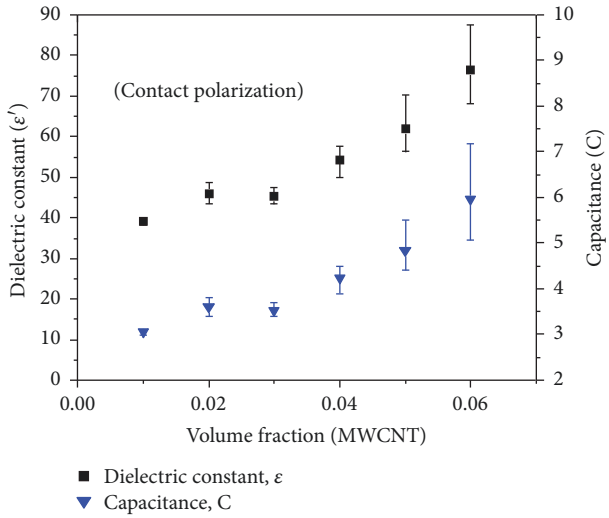

Figure 12: The capacitance, C, and dielectric constant, ε', of three-phase PZT-Epoxy-MWCNT thick films that were contact polarized, plotted as a function of MWCNT volume fraction, show an enhancement in the values with an increase in the volume fraction of MWCNT at 110 Hz.

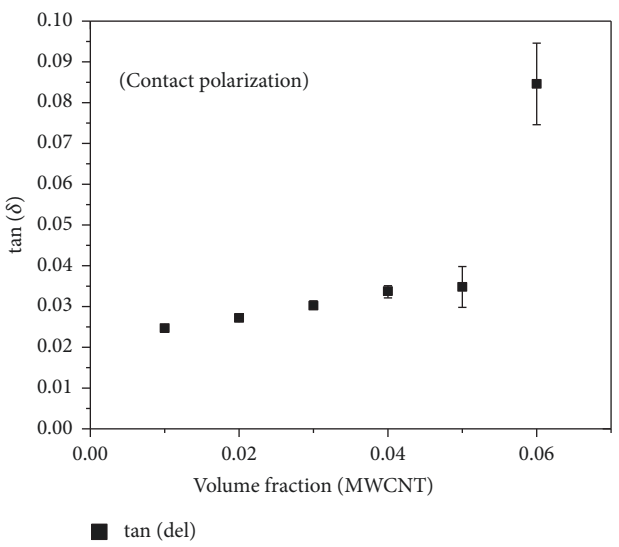

Figure 13: Tangent of the loss angle, tan (δ) of the three-phase composite, increases with increasing volume fraction of MWCNTs.

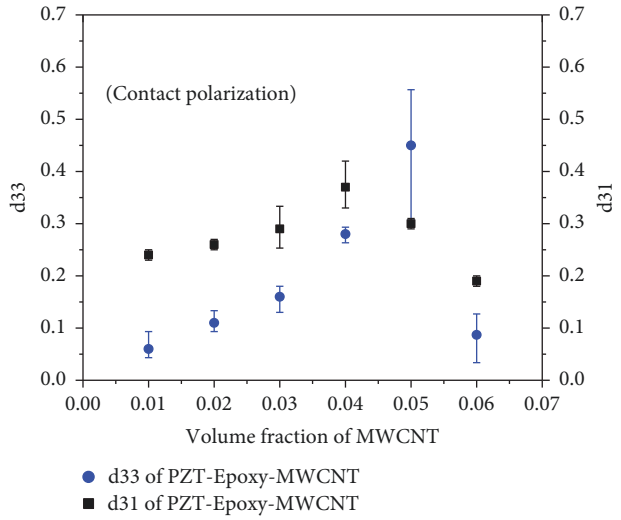

Figure 14: Piezoelectric strain coefficients, d_{33} and d_{31}, of three-phase PZT-epoxy-MWCNT thick films that were polarized via the parallel-plate contact method. The strain coefficients increase with the volume fraction of MWCNTs.

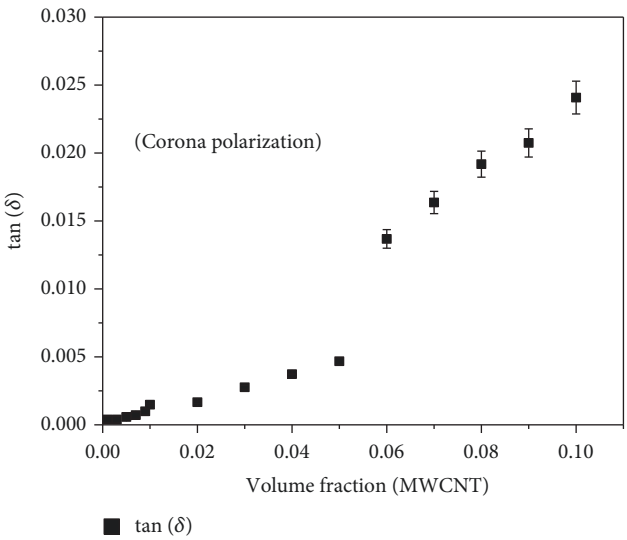

Figure 15: Tangent of the loss angle, tan (δ) of the three-phase composite, increases with increasing volume fraction of MWCNTs.

the 33-direction, is also enhanced due to the increase in the number of the dipoles aligned along the 33-direction.

The conductivity values for bulk and thick film composites of the same composition are shown in Figures 18 and 19 for contact and corona polarized composites, respectively. The conductivity increased with the volume fraction of the MWCNTs, which is due to the increase in the formation of conductive pathways in the composite and electron transport through electron tunneling in the composites. In Figure 18, an increase in the conductivity values is seen for the contact polarized composites, for a change in MWCNT volume fraction from 5 to 6%, i.e., from 0.10 to 0.25 μS/m and 0.0.07 to 0.16 μS/m for the bulk and thick film composites, respectively. Also, in Figure 19, a similar sharp increase in conductivity occurs from 0.17 to 0.69 μS/m and from 0.10 to 0.77 μS/m for the bulk and thick films, respectively, for a change in MWCNT volume fraction from 5 to 6%. This marked increase in the conductivity of both bulk and thick film composites indicates that they reach the percolation region around a MWCNT volume fraction of 5-6%. This is evidenced by an increase in the dielectric constant and the piezoelectric strain coefficients with an increase in the volume fraction of the MWCNT inclusions below the percolation limit and sharp increase in the dielectric constant, and the dielectric loss is observed due the formation of percolation pathways in the composites. A comparison of piezoelectric and dielectric properties based on corona and contact

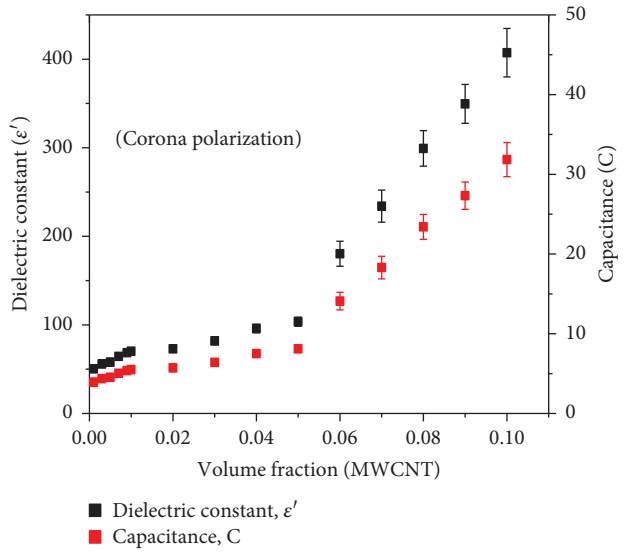

Figure 16: Capacitance and dielectric constant that were polarized via a corona discharge technique are plotted as a function of increasing MWCNT volume fraction, wherein each increase with MWCNT content.

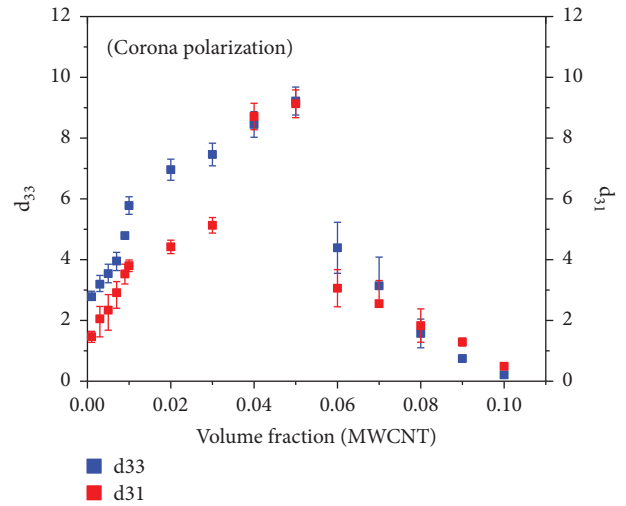

Figure 17: Piezoelectric strain coefficients, d_{33} and d_{31}, of the films that were corona polarized are plotted as a function of MWCNT volume fraction. The piezoelectric strain coefficients increase with the MWCNT volume fraction content.

poling shows that the corona discharge polarization is more efficient than the contact poling method.

4. Conclusions

Nanocomposite thick films have been fabricated that include piezoelectric PZT, epoxy, and MWCNTs. An investigation of the surface processing of the MWCNTs and polarization technique was explored. It was determined that the corona polarization technique was more effective than the contact polarization process. Sharp decreases in the impedance and sharp increases in the conductivity of the composites indicated the percolation region. The percolation region

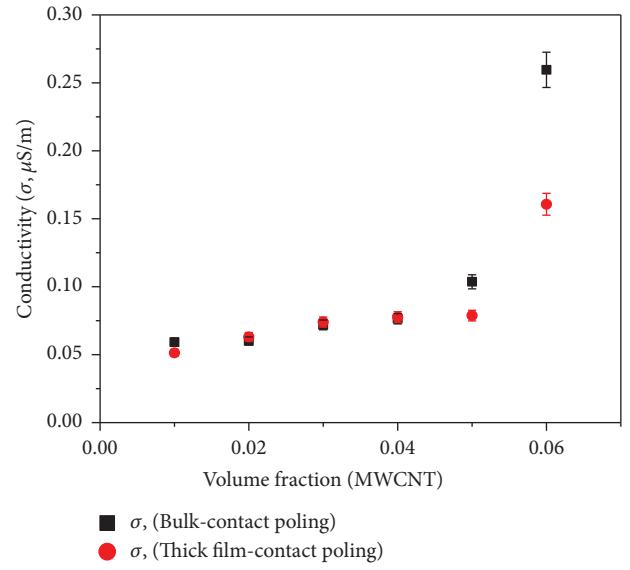

Figure 18: Conductivity measurements at 2 kHz for (A) corona poled and (B) contact poled bulk and thick film composites show a sharp rise in the values around a MWCNT volume fraction change from 5 to 6% which is predicted to be the region of percolation threshold from the previous piezoelectric and dielectric characteristics of the composites.

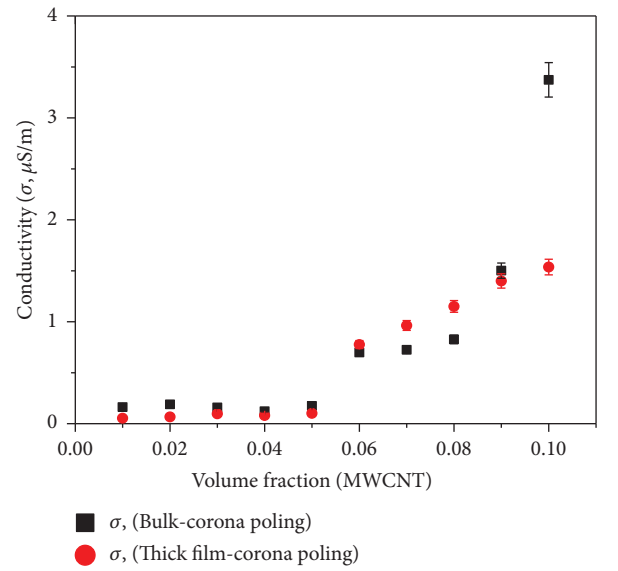

Figure 19: Conductivity measurements at 2 kHz for (A) corona poled and (B) contact poled bulk and thick film composites show a sharp rise in the values around a MWCNT volume fraction change from 5 to 6% which is predicted to be the region of percolation threshold from the previous piezoelectric and dielectric characteristics of the composites.

was similar to that observed by Shehzad et al. [80]. Interfacial interaction plays a major role in determining the material properties of the thick film composites [83], wherein the addition of PZT and MWCNTs enhances the interfacial contact resistance that leads to increases in the capacitance and ultimately the permittivity of the composites. Microstructural interactions such as these between the conductive

inclusions, the matrix material, and the piezoelectric phase [32, 41] influence the effective properties of the composite.

Data Availability

The data used to support the findings of this study are available from the corresponding author upon request.

Conflicts of Interest

The authors declare that they have no conflicts of interest.

Acknowledgments

This material is based upon work supported by the National Science Foundation under Grant numbers EEC1659818, EEC1263250, and EEC1407266. In addition, we would like to acknowledge the support from the New Jersey Space Grant Consortium.

References

[1] E. P. Scala, "A brief history of composites in the U.S.—the dream and the success," *JOM*, vol. 48, no. 2, pp. 45–48, 1996.

[2] A. Saigal, A. E. Giannakopoulos, and S. Suresh, "Parametric study of the volume fraction of fibers in 1-3 PZT/polyurethane piezoelectric composites during indentation," *Ferroelectrics*, vol. 255, no. 1, pp. 1–12, 2001.

[3] G. H. Haertling, "Ferroelectric ceramics: history and technology," *Journal of the American Ceramic Society*, vol. 82, no. 4, pp. 797–818, 1999.

[4] H. Tong, Y. Li, L. Zhang, and B. Li, "Mechanism design and process control of micro EDM for drilling spray holes of diesel injector nozzles," *Precision Engineering*, vol. 37, no. 1, pp. 213–221, 2013.

[5] P. M. Weaver, T. Stevenson, T. Quast et al., "High temperature measurement and characterisation of piezoelectric properties," *Journal of Materials Science: Materials in Electronics*, vol. 26, no. 12, pp. 9268–9278, 2015.

[6] S. Banerjee and K. A. Cook-Chennault, "Influence of Al particle size and lead zirconate titanate (PZT) volume fraction on the dielectric properties of PZT-epoxy-aluminum composites," *Journal of Engineering Materials and Technology*, vol. 133, no. 4, article 041016, 2011.

[7] U. Aridogan, I. Basdogan, and A. Erturk, "Analytical modeling and experimental validation of a structurally integrated piezoelectric energy harvester on a thin plate," *Smart Materials and Structures*, vol. 23, no. 4, article 045039, 2014.

[8] U. Boz and I. Basdogan, "IIR filtering based adaptive active vibration control methodology with online secondary path modeling using PZT actuators," *Smart Materials and Structures*, vol. 24, no. 12, article 125001, 2015.

[9] J. Jiang, Y. Bitla, C. W. Huang et al., "Flexible ferroelectric element based on van der Waals heteroepitaxy," *Science Advances*, vol. 3, no. 6, article e1700121, 2017.

[10] M. Lethiecq, F. Levassort, D. Certon, and L. Tran-Huu-Hue, "Piezoelectric transducer design for medical diagnosis and NDE," in *Piezoelectric and Acoustic Materials for Transducer Applications*, A. Safari and E. K. Akdoğan, Eds., pp. 191–215, Springer US, Boston, MA, USA, 2008.

[11] T. Bove, W. Wolny, E. Ringgaard, and A. Pedersen, "New piezoceramic PZT-PNN material for medical diagnostics applications," *Journal of the European Ceramic Society*, vol. 21, no. 10-11, pp. 1469–1472, 2001.

[12] M. Li, J. Yuan, D. Guan, and W. Chen, "Application of piezoelectric fiber composite actuator to aircraft wing for aerodynamic performance improvement," *Science China Technological Sciences*, vol. 54, no. 2, pp. 395–402, 2011.

[13] H. Miao, Q. Huan, Q. Wang, and F. Li, "Excitation and reception of single torsional wave $T(0,1)$ mode in pipes using face-shear d24 piezoelectric ring array," *Smart Materials and Structures*, vol. 26, no. 2, article 025021, 2017.

[14] A. A. H. S. Shirazi, F. Mustapha, and K. A. Ahmad, "Damage identification using wireless structural health monitoring system through smart sensor application," *International Journal of Advanced and Applied Sciences*, vol. 4, no. 2, pp. 38–43, 2017.

[15] M. Rosiek, A. Martowicz, and T. Uhl, "Electromechanical impedance based SHM system for aviation applications," *Key Engineering Materials*, vol. 518, pp. 127–136, 2012.

[16] B. McClarren and R. Olabisi, "Strain and vibration in mesenchymal stem cells," *International Journal of Biomaterials*, vol. 2018, Article ID 8686794, 13 pages, 2018.

[17] S. Chalasani and J. M. Conrad, "A survey of energy harvesting sources for embedded systems," in *IEEE SoutheastCon 2008*, pp. 442–447, Huntsville, AL, USA, April 2008.

[18] T. Kim, A. I. Kingon, J. P. Maria, and R. T. Croswell, "Lead zirconate titanate thin film capacitors on electroless nickel coated copper foils for embedded passive applications," *Thin Solid Films*, vol. 515, no. 18, pp. 7331–7336, 2007.

[19] A. Wu, P. M. Vilarinho, and A. I. Kingon, "Electrophoretic deposition of lead zirconate titanate films on metal foils for embedded components," *Journal of the American Ceramic Society*, vol. 89, no. 2, pp. 575–581, 2006.

[20] A. S. Khan and W. G. Proud, "Temperature and strain rate effects on the piezoelectric charge production of PZT 95/5," in *Shock Compression of Condensed Matter - 2015. vol. 1793*, R. Chau, T. Germann, I. Oleynik, S. Peiris, R. Ravelo, and T. Sewell, Eds., Puertollano, Spain, 2017.

[21] M. C. Robinson and D. F. Bahr, "Failure strains in micromachined piezoelectric membranes," *Strain*, vol. 45, no. 1, pp. 55–62, 2009.

[22] S. Wang and K. X. Liu, "Experimental research on dynamic mechanical properties of PZT ceramic under hydrostatic pressure," *Materials Science and Engineering: A*, vol. 528, no. 21, pp. 6463–6468, 2011.

[23] A. Mazzalai, D. Balma, N. Chidambaram, P. Murat, and L. Colombo, "Dynamic and long-time tests of the transverse piezoelectric coefficient in PZT thin films," in *2014 Joint IEEE International Symposium on the Applications of Ferroelectric, International Workshop on Acoustic Transduction Materials and Devices & Workshop on Piezoresponse Force Microscopy*, pp. 162–165, State College, PA, USA, May 2014.

[24] K. A. Cook-Chennault, D. Cosaboon, D. Eigbe, B. Pitcavage, M. Whitzer, and D. Castley, "Enhanced output voltage and power from conductive inclusions in A 0–3-0 piezoelectric composite," in *ASME 2010 International Mechanical Engineering Congress and Exposition*, pp. 61–64, Vancouver, British Columbia, Canada, November 2010.

[25] K. A. Cook-Chennault, N. Thambi, and A. M. Sastry, "Powering MEMS portable devices—a review of non-regenerative and

regenerative power supply systems with special emphasis on piezoelectric energy harvesting systems," *Smart Materials and Structures*, vol. 17, no. 4, article 043001, 2008.

[26] Z. Y. Hu, L. P. Li, J. J. Zhou, and L. Li, "Preparation and performance of inorganic composite separators for lithium-ion battery," *Acta Polymerica Sinica*, pp. 1288–1293, 2015.

[27] S. Banerjee and K. A. Cook-Chennault, "An analytical model for the effective dielectric constant of a 0-3-0 composite," *Journal of Engineering Materials and Technology*, vol. 133, no. 4, article 041005, 2011.

[28] S. Banerjee and K. A. Cook-Chennault, "An investigation into the influence of electrically conductive particle size on electromechanical coupling and effective dielectric strain coefficients in three phase composite piezoelectric polymers," *Composites Part A: Applied Science and Manufacturing*, vol. 43, no. 9, pp. 1612–1619, 2012.

[29] S. Banerjee and K. A. Cook-Chennault, "Influence of aluminium inclusions on dielectric properties of three-phase PZT-cement-aluminium composites," *Advances in Cement Research*, vol. 26, no. 2, pp. 63–76, 2014.

[30] S. Banerjee, K. A. Cook-Chennault, W. Du, U. Sundar, H. Halim, and A. Tang, "Piezoelectric and dielectric characterization of corona and contact poled PZT-epoxy-MWCNT bulk composites," *Smart Materials and Structures*, vol. 25, no. 11, article 115018, 2016.

[31] S. Banerjee, W. Du, L. Wang, and K. A. Cook-Chennault, "Fabrication of dome-shaped PZT-epoxy actuator using modified solvent and spin coating technique," *Journal of Electroceramics*, vol. 31, no. 1-2, pp. 148–158, 2013.

[32] S. Banerjee, R. Kappera, M. Chhowalla, and K. A. Cook-Chennault, "Multi walled carbon nanotube based flexible multi-morph composite thick films with graphene electrodes," *Energy and Environmental Focus*, vol. 2, no. 3, pp. 195–202(8), 2013.

[33] S. Banerjee, J. Torres, and K. A. Cook-Chennault, "Piezoelectric and dielectric properties of PZT-cement-aluminum nano-composites," *Ceramics International*, vol. 41, no. 1, pp. 819–833, 2015.

[34] H.-W. Choi, Y. W. Heo, J. H. Lee et al., "Effects of $BaTiO_3$ on dielectric behavior of $BaTiO_3$–Ni–polymethyl methacrylate composites," *Applied Physics Letters*, vol. 89, no. 13, article 132910, 2006.

[35] K. Arlt and M. Wegener, "Piezoelectric PZT / PVDF-copolymer 0-3 composites: aspects on film preparation and electrical poling," *IEEE Transactions on Dielectrics and Electrical Insulation*, vol. 17, no. 4, pp. 1178–1184, 2010.

[36] D.-H. Kuo, C.-C. Chang, T.-Y. Su, W.-K. Wang, and B.-Y. Lin, "Dielectric behaviours of multi-doped $BaTiO_3$/epoxy composites," *Journal of the European Ceramic Society*, vol. 21, no. 9, pp. 1171–1177, 2001.

[37] V. Pascariu, L. Padurariu, O. Avadanei, and L. Mitoseriu, "Dielectric properties of PZT–epoxy composite thick films," *Journal of Alloys and Compounds*, vol. 574, pp. 591–599, 2013.

[38] C. Chen, R. Zhang, Z. Wang, and W. Cao, "Electromechanical coupling coefficient k_{eff}^{31} for arbitrary aspect ratio resonators made of [001] and [011] poled $(1-x)Pb(Mg_{1/3}Nb_{2/3})O_3$–$xPbTiO_3$ single crystals," *Journal of Applied Physics*, vol. 105, no. 6, article 064104, 2009.

[39] S. C. Stein, C. Liang, and C. A. Rogers, "Power consumption of piezoelectric actuators driving a simply supported beam considering fluid coupling," *The Journal of the Acoustical Society of America*, vol. 96, no. 3, pp. 1598–1604, 1994.

[40] J. A. Mapkar, A. Belashi, L. M. Berhan, and M. R. Coleman, "Formation of high loading flexible carbon nanofiber network composites," *Composites Science and Technology*, vol. 75, pp. 1–6, 2013.

[41] Z.-M. Dang, S.-H. Yao, J.-K. Yuan, and J. Bai, "Tailored dielectric properties based on microstructure change in $BaTiO_3$-carbon nanotube/polyvinylidene fluoride three-phase nanocomposites," *The Journal of Physical Chemistry C*, vol. 114, no. 31, pp. 13204–13209, 2010.

[42] H. Gong, Y. Zhang, J. Quan, and S. Che, "Preparation and properties of cement based piezoelectric composites modified by CNTs," *Current Applied Physics*, vol. 11, no. 3, pp. 653–656, 2011.

[43] A. Seema, K. R. Dayas, and J. M. Varghese, "PVDF-PZT-5H composites prepared by hot press and tape casting techniques," *Journal of Applied Polymer Science*, vol. 106, no. 1, pp. 146–151, 2007.

[44] R. Senthilkumar, K. Sridevi, J. Venkatesan, V. Annamalai, and M. S. Vijaya, "Investigations on ferroelectric PZT-PVDF composites of 0–3 connectivity," *Ferroelectrics*, vol. 325, no. 1, pp. 121–130, 2005.

[45] B. Satish, K. Sridevi, and M. S. Vijaya, "Study of piezoelectric and dielectric properties of ferroelectric PZT-polymer composites prepared by hot-press technique," *Journal of Physics D: Applied Physics*, vol. 35, no. 16, pp. 2048–2050, 2002.

[46] Y. Song, Z. Zhao, W. Yu, B. Li, and X. Chen, "Morphological structures of poly(vinylidene fluoride)/montmorillonite nanocomposites," *Science in China Series B: Chemistry*, vol. 50, no. 6, pp. 790–796, 2007.

[47] Y. Dan, Y. Lu, N. J. Kybert, Z. Luo, and A. T. C. Johnson, "Intrinsic response of graphene vapor sensors," *Nano Letters*, vol. 9, no. 4, pp. 1472–1475, 2009.

[48] Y. Bai, Z. Y. Cheng, V. Bharti, H. S. Xu, and Q. M. Zhang, "High-dielectric-constant ceramic-powder polymer composites," *Applied Physics Letters*, vol. 76, no. 25, pp. 3804–3806, 2000.

[49] Z. Li, B. Dong, and D. Zhang, "Influence of polarization on properties of 0–3 cement-based PZT composites," *Cement and Concrete Composites*, vol. 27, no. 1, pp. 27–32, 2005.

[50] M. Thomas, K. Folliard, T. Drimalas, and T. Ramlochan, "Diagnosing delayed ettringite formation in concrete structures," *Cement and Concrete Research*, vol. 38, no. 6, pp. 841–847, 2008.

[51] K. Yadav, C. W. Smelser, S. Jacob, C. Blanchetiere, C. L. Callender, and J. Albert, "Simultaneous corona poling of multiple glass layers for enhanced effective second-order optical nonlinearities," *Applied Physics Letters*, vol. 99, no. 3, article 031109, 2011.

[52] L. Qi, B. I. Lee, W. D. Samuels, G. J. Exarhos, and S. G. Parler, "Three-phase percolative silver–$BaTiO_3$–epoxy nanocomposites with high dielectric constants," *Journal of Applied Polymer Science*, vol. 102, no. 2, pp. 967–971, 2006.

[53] L.-y. Zhao, J.-g. Guan, H.-r. Ma, and Z.-g. Sun, "Mechanical properties and curing kinetics of epoxy resins cured by various amino-terminated polyethers," *Chinese Journal of Polymer Science*, vol. 28, no. 6, pp. 961–969, 2010.

[54] S.-H. Yao, Z.-M. Dang, M.-J. Jiang, and J. Bai, "$BaTiO_3$-carbon nanotube/polyvinylidene fluoride three-phase composites with high dielectric constant and low dielectric loss," *Applied Physics Letters*, vol. 93, no. 18, article 182905, 2008.

[55] Z. M. Dang, Y. Shen, and C. W. Nan, "Dielectric behavior of three-phase percolative Ni–$BaTiO_3$/polyvinylidene fluoride composites," *Applied Physics Letters*, vol. 81, no. 25, pp. 4814–4816, 2002.

[56] Z. Wang, J. K. Nelson, J. Miao et al., "Effect of high aspect ratio filler on dielectric properties of polymer composites: a study on barium titanate fibers and graphene platelets," *IEEE Transactions on Dielectrics and Electrical Insulation*, vol. 19, no. 3, pp. 960–967, 2012.

[57] S. L. Kok, N. M. White, and N. R. Harris, "Free-standing thick-film piezoelectric device," *Electronics Letters*, vol. 44, no. 4, p. 280, 2008.

[58] V. Sencadas, S. Lanceros-Mendez, R. G. Filho, D. L. Chinaglia, and A. S. Pouzada, "Influence of the processing conditions and corona poling on the morphology of β-PVDF," in *2005 12th International Symposium on Electrets*, pp. 161–164, Salvador, Brazil, September 2005.

[59] Y. Shen, Y. Guan, Y. Hu et al., "Dielectric behavior of graphene/$BaTiO_3$/polyvinylidene fluoride nanocomposite under high electric field," *Applied Physics Letters*, vol. 103, no. 7, article 072906, 2013.

[60] X. Zeng, X. Xu, P. M. Shenai et al., "Characteristics of the electrical percolation in carbon nanotubes/polymer nanocomposites," *The Journal of Physical Chemistry C*, vol. 115, no. 44, pp. 21685–21690, 2011.

[61] G. Gao, T. Çagin, and W. A. Goddard III, "Energetics, structure, mechanical and vibrational properties of single-walled carbon nanotubes," *Nanotechnology*, vol. 9, no. 3, pp. 184–191, 1998.

[62] O. Deriabina, N. Lebovka, L. Bulavin, and A. Goncharuk, "Regulation of dispersion of carbon nanotubes in binary water+1-cyclohexyl-2-pyrrolidone mixtures," *Physica E: Low-Dimensional Systems & Nanostructures*, vol. 59, pp. 150–157, 2014.

[63] S. Maiti, S. Suin, N. K. Shrivastava, and B. B. Khatua, "Low percolation threshold in melt-blended PC/MWCNT nanocomposites in the presence of styrene acrylonitrile (SAN) copolymer: preparation and characterizations," *Synthetic Metals*, vol. 165, pp. 40–50, 2013.

[64] J. P. Peng, H. Zhang, L. C. Tang, Y. Jia, and Z. Zhang, "Dielectric properties of carbon nanotubes/epoxy composites," *Journal of Nanoscience and Nanotechnology*, vol. 13, no. 2, pp. 964–969, 2013.

[65] W. D. Jenkins, T. G. Digges, and C. R. Johnson, "Tensile properties of copper, nickel, and 70-percent-Copper-30-percent-nickel and 30-percent-copper- 70-percent nickel alloys at high temperatures," *Journal of Research of the National Bureau of Standards*, vol. 58, no. 4, pp. 201–211, 1957.

[66] R. H. Baughman, A. A. Zakhidov, and W. A. de Heer, "Carbon nanotubes–the route toward applications," *Science*, vol. 297, no. 5582, pp. 787–792, 2002.

[67] J. M. Harris, G. R. S. Iyer, A. K. Bernhardt et al., "Electronic durability of flexible transparent films from type-specific single-wall carbon nanotubes," *ACS Nano*, vol. 6, no. 1, pp. 881–887, 2012.

[68] G. R. Headifen and E. P. Fahrenthold, "Mechanical and electrical-properties of glass and carbon fiber-reinforced composites," *Journal of Energy Resources Technology*, vol. 113, no. 3, pp. 176–181, 1991.

[69] B. Zidlicky, J. Marik, and M. Jandera, "Cold-forming effect on mechanical properties of stainless steel section - material testing," *Engineering Mechanics 2016*, I. Zolotarev and V. Radolf, Eds., pp. 634–637, Korean Society of Steel Construction, 2016.

[70] A. Guldas, M. Altug, and S. Temel, "Mechanical properties of aluminum powder reinforced polypropylene," *Materials Testing*, vol. 59, no. 1, pp. 86–93, 2017.

[71] I. H. Tavman, "Thermal and mechanical properties of aluminum powder-filled high-density polyethylene composites," *Journal of Applied Polymer Science*, vol. 62, no. 12, pp. 2161–2167, 1996.

[72] M. C. Hermant, *Manipulating the Percolation Threshold of Carbon Nanotubes in Polymeric Composites*, Doctor of Philosophy, Technische Universiteit Eindhoven, Technische Universiteit Eindhoven, 2009.

[73] Z. Ounaies, C. Park, J. Harrison, and P. Lillehei, "Evidence of piezoelectricity in SWNT-polyimide and SWNT-PZT-polyimide composites," *Journal of Thermoplastic Composite Materials*, vol. 21, no. 5, pp. 393–409, 2008.

[74] J. Arsecularatne and L. Zhang, "Carbon nanotube reinforced ceramic composites and their performance," *Recent Patents on Nanotechnology*, vol. 1, no. 3, pp. 176–185, 2007.

[75] S. Tian and X. Wang, "Fabrication and performances of epoxy/multi-walled carbon nanotubes/piezoelectric ceramic composites as rigid piezo-damping materials," *Journal of Materials Science*, vol. 43, no. 14, pp. 4979–4987, 2008.

[76] V. Leon, R. Parret, R. Almairac et al., "Spectroscopic study of double-walled carbon nanotube functionalization for preparation of carbon nanotube / epoxy composites," *Carbon*, vol. 50, no. 14, pp. 4987–4994, 2012.

[77] M. Heimann, M. Wirts-Ruetters, B. Boehme, and K. J. Wolter, "Investigations of carbon nanotubes epoxy composites for electronics packaging," in *2008 58th Electronic Components and Technology Conference*, pp. 1731–1736, Lake Buena Vista, FL, USA, May 2008.

[78] B. Wang, L. Liu, L. Huang et al., "Fabrication and origin of high-k carbon nanotube/epoxy composites with low dielectric loss through layer-by-layer casting technique," *Carbon*, vol. 85, pp. 28–37, 2015.

[79] M. Haghgoo, A. A. Yousefi, M. J. Z. Mehr et al., "Correlation between morphology and electrical conductivity of dried and carbonized multi-walled carbon nanotube/resorcinol-formaldehyde xerogel composites," *Journal of Materials Science*, vol. 50, no. 18, pp. 6007–6020, 2015.

[80] K. Shehzad, M. N. Ahmad, T. Hussain et al., "Influence of carbon nanotube dimensions on the percolation characteristics of carbon nanotube/polymer composites," *Journal of Applied Physics*, vol. 116, no. 6, article 064908, 2014.

[81] J. H. Sandoval, K. F. Soto, L. E. Murr, and R. B. Wicker, "Nanotailoring photocrosslinkable epoxy resins with multi-walled carbon nanotubes for stereolithography layered manufacturing," *Journal of Materials Science*, vol. 42, no. 1, pp. 156–165, 2007.

[82] J. H. Sandoval and R. B. Wicker, "Functionalizing stereolithography resins: effects of dispersed multi-walled carbon nanotubes on physical properties," *Rapid Prototyping Journal*, vol. 12, no. 5, pp. 292–303, 2006.

[83] M. Akiyama, Y. Morofuji, T. Kamohara et al., "Flexible piezoelectric pressure sensors using oriented aluminum nitride thin films prepared on polyethylene terephthalate films," *Journal of Applied Physics*, vol. 100, no. 11, pp. 114318–114315, 2006.


The Scientific
World Journal
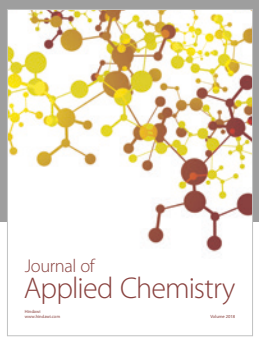
Journal of
Applied Chemistry
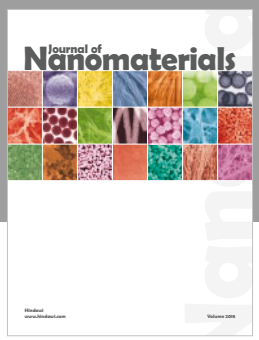
Journal of
Nanomaterials

Scientifica

International Journal of
Polymer Science
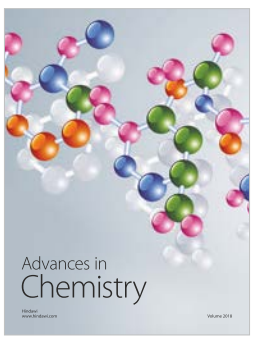
Advances in
Chemistry

Hindawi
Submit your manuscripts at
www.hindawi.com
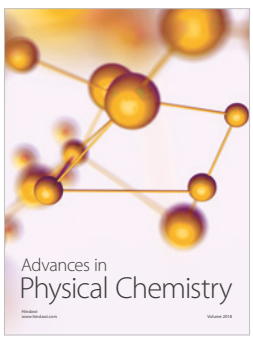
Advances in
Physical Chemistry

International Journal of
Analytical Chemistry
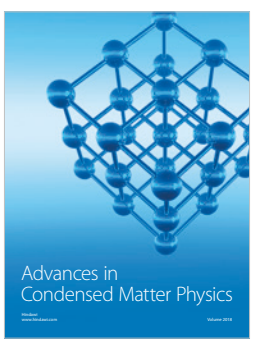
Advances in
Condensed Matter Physics
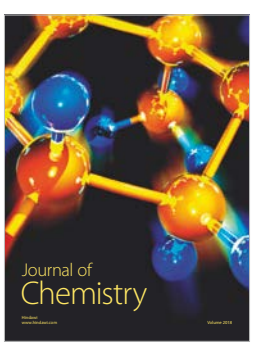
Journal of
Chemistry

International Journal of
Biomaterials
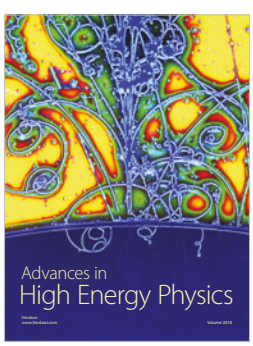
Advances in
High Energy Physics

Journal of
Engineering

Journal of
Nanotechnology

International Journal of
Corrosion

Journal of
Materials

BioMed
Research International
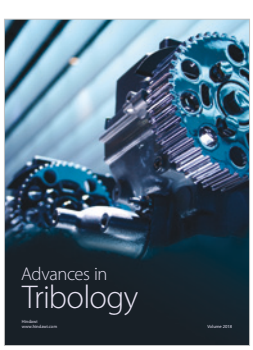
Advances in
Tribology
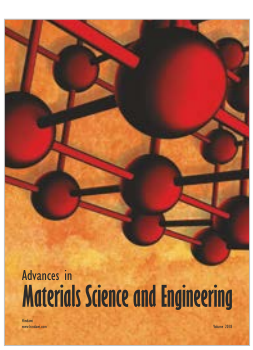
Advances in
Materials Science and Engineering